Quim. Nova, Vol. 48, No. 7, e-20250155, 1-10, 2025 http://dx.doi.org/10.21577/0100-4042.20250155

Article

SYNTHESIS OF THE TiO_2/g-C_3N_4 PHOTOCATALYST AND ITS PHOTOCATALYTIC PERFORMANCE FOR SELECTIVE OXIDATION OF ALCOHOLS

Shuangyan Meng[a], Bin Liu[a], Minglin Xie[a], Chaoxin Yun[a], Jin Qiang[a], Kaizhou He[a], Zhiwang Yang[b] and Xiangqian Wang[a,*]

[a]Key Laboratory of Sensor and Sensing Technology, Institute of Sensing Technology, Gansu Academy of Sciences, 730000 Lanzhou, China

[b]Key Laboratory of Eco-Functional Polymer Materials, Ministry of Education, Key Laboratory of Eco-Environmental Polymer Materials of Gansu Province, College of Chemistry and Chemical Engineering, Northwest Normal University, 730070 Lanzhou, China

Received: 11/19/2024; accepted: 04/29/2025; published online: 06/13/2025

A composite photocatalyst, xTCN (x$OTiO_2$/g-C_3N_4, where x represents the added quantity of graphite carbon nitride (g-C_3N_4)), was synthesized using a straightforward one-step hydrothermal method with H_2O_2 as an oxidant. The H_2O_2 incorporation into the xTCN composite facilitated the enrichment of oxygen (O) in titanium dioxide (TiO_2). This synthesis process effectively reduced the bandgap energy, minimizing the recombination of photogenerated carriers. Concurrently, an O atom was integrated into the g-C_3N_4 molecule, which altered its bandgap structure and enhanced the photogenerated electron-hole separation efficiency. The dual modification effect was observed when 0.9TCN was used as the catalyst, which converted 77% of benzalcohol with a selectivity exceeding 99%. Additionally, five cycles of reuse only slightly decreased the benzalcohol conversion (by 16%) and selectivity (by 9%), indicating good reusability of the xTCN photocatalyst. The xTCN photocatalyst had an unchanged molecular structure before and after the photocatalytic reaction, demonstrating its superior light stability. The potential photocatalytic reaction mechanism was explored through an active species capture experiment and a Mott-Schottky (M-S) curve test. The results of these studies suggested that $\bullet O_2^-$ and •OH were the primary reactive species in the photocatalytic reaction.

Keywords: TiO_2; g-C_3N_4; visible light catalysis; selective oxidation of alcohol.

INTRODUCTION

Benzaldehyde is a crucial intermediate or precursor in various industries, including spices, dyes, additives, medicines, and agricultural chemicals.[1] The selective oxidation of alcohols to their corresponding aldehydes or ketones is a significant chemical process in industrial applications and fundamental organic transformations.[2,3] Consequently, the chemical industry has shown significant interest in synthesizing benzaldehyde efficiently. Conventional industries typically employ costly metal salts as oxidants to oxidize alcohols to aldehydes. Additionally, this approach complicates the separation of the products and inevitably generates hazardous waste.[4] Therefore, devising a sustainable, eco-friendly, and efficient approach for selectively oxidizing alcohols to their corresponding aldehydes is a pressing requirement as an alternative to traditional methods. Among the myriad methodologies available, photocatalytic technology is the most potent technique for the selective oxidation of alcohols.

Titanium dioxide (TiO_2), a characteristic semiconductor with a wide energy gap of 3.2 eV, is activated solely by ultraviolet (UV) light. Moreover, UV light constitutes only 4% of the incident solar energy on the surface of the Earth and has a wavelength range of less than 400 nm ($\lambda = hc/E_g$), making its effective utilization for solar energy applications challenging.[5] Due to its superior inherent electronic and surface properties, TiO_2 is widely recognized as the most versatile and promising semiconductor photocatalyst. Moreover, TiO_2 offers several advantages, including low cost, non-toxicity, abundant reserves, unique photoelectric performance, chemical stability, and thermal stability.[6,7] Therefore, it is extensively employed in various applications, such as photocatalytic hydrogen production,[8] CO_2 reduction,[9] degradation of organic pollutants,[10] sodium-ion battery materials,[11] mutual conversion of organic compounds,[12,13] and photoelectrocatalytic water cracking for hydrogen production.[14] Factors, such as specific surface area, size, morphology, pore structure and volume, crystal phase, defect state, exposed crystal plane characteristics, and surface potential, predominantly influenced the photocatalytic performance of TiO_2.[15] Several techniques, including transition metal deposition,[16,17] doping with metal ions[18] or non-metallic ions,[19] and coupling with narrow band gap semiconductors,[20] are employed to enhance the response of TiO_2 to visible light, improving the efficiency of solar energy utilization. However, the current effect is not ideal, necessitating further studies to identify promising photocatalytic materials that can rival TiO_2, which would expand the range of TiO_2 applications.

Graphite carbon nitride (g-C_3N_4), a free-metal, graphene-like photocatalytic material, has garnered significant attention due to its high stability, low cost, non-toxicity, suitable band position, and excellent photoelectric performance.[21] It can be synthesized using inexpensive precursors, such as urea, dicyandiamide, and melamine, through thermal polymerization.[22] However, the g-C_3N_4 surface has rapid photogenerated carrier recombination due to the weak van der Waals force within the molecule, resulting in poor separation of photogenerated electrons and holes.[23] Prevalent strategies to address the inherent limitations of the g-C_3N_4 molecule and to improve the transfer efficiency of photogenerated carriers include metal and non-metal ion doping,[24] precious metal deposition,[25] surface modification,[26] and coupling with other semiconductors.[27]

Previously, An and co-authors[28,29] extensively studied the applications of TiO_2/g-C_3N_4 materials. They used hydrothermal calcination to synthesize a TiO_2/g-C_3N_4 hybrid photocatalyst with a

*e-mail: wxiangqian_1987@163.com

Associate Editor handled this article: Boniek G. Vaz

high catalytic activity, which was applied to study the bactericidal properties and toxicity of drug degradation intermediates under visible light irradiation. The results indicated that the hybrid photocatalyst had a high catalytic activity due to the synergistic effect of TiO_2 and g-C_3N_4, and this finding had significant implications for water sterilization and purification.

This study synthesized the xTCN composite photocatalyst using a straightforward one-step hydrothermal technique. The synthesized materials were comprehensively characterized using various methods to meticulously examine their structure, morphology, optical properties, and electrical attributes. The findings indicated that variations in the g-C_3N_4 quantities corresponded to differences in the photocatalytic activity. Even minute quantities of g-C_3N_4 enhanced the photo-responsiveness of TiO_2, which significantly improved the photogenerated electron-hole separation efficiency and substantially enhanced the photocatalytic performance. The photocatalytic performance of the xTCN composite photocatalyst was examined using the selective oxidation of benzalcohol as a model reaction. Under conditions of oxygen (O) and light, 77% of benzalcohol was converted, with a selectivity exceeding 99%. Mechanistic investigations revealed that $\bullet O_2^-$ and •OH were the primary active species in the photocatalytic reaction system.

EXPERIMENTAL

Chemicals and reagents

Tetra-butyl titanate (TBOT), urea, hydrogen peroxide (H_2O_2, 30%), sodium sulfite (Na_2SO_3), sodium sulfate (Na_2SO_4), and isopropanol (IPA) were procured from Sinophenol Chemical Reagent Co., Ltd. Silver nitrate ($AgNO_3$) and *p*-benzoquinone (BQ) were obtained from Shanghai Fine Chemical Materials Research Institute and Saan Chemical Technology Co., Ltd, respectively. TEMPO (2,2,6,6-tetramethyl-1-piperidinyloxy) was purchased from Aladdin Scientific. Benzalcohol and its derivatives were obtained from Aladdin Scientific and Bellingway Technology Co., Ltd. Carbon tetrachloride (CCl_4) and 1,2-dichloroethane were acquired from the Beijing Chemical Plant. Ethyl acetate, anhydrous ethanol, toluene, tetrahydrofuran, acetonitrile, and hexane were sourced from Tianjin Chemical Reagent Factory. Moreover, all reagents were obtained through commercial channels.

Characterization

An X-ray diffractometer (D/Max 2400 type, Rigaku, Japan) was utilized for X-ray powder diffraction (XRD). The radiation source was Cu Kα, with a 5° scanning speed and a 2θ scanning range of 5-80°. The wavelength (λ) parameter, the tube voltage, and the tube current were 1.5418 Å, 40 kV, and 100 Ma, respectively. The Fourier transform infrared (FTIR) spectra were obtained using a Fourier transform infrared spectrometer (PerkinElmer, USA), which used KBr as the reference sample and employed the solid pressure method, with a test range of 4000-400 cm^{-1}. A multifunctional electron spectrometer (Thermo ESCALAB 250XI, Physical Electronics, USA) was used for X-ray photoelectron spectroscopy (XPS). The analysis range extended from Li to U, with an analysis area of 30 μm^2-0.8 × 2 mm^2. The X-ray emission source consisted of a Mg, Al double anode target and an Al monochromator target. A thermal field emission scanning electron microscope (Ultra Plus, Germany Chase) was used for scanning electron microscopy (SEM). The scanning electron microscope offered a 12-900000× magnification range and voltages between 0.1 and 30 kV, determining the content and element distribution of the samples. Additionally, a spraying machine (108 Auto, Cressington, Au, Pt) was used. This experiment used a physical adsorption apparatus (autosorb-IQ^2-MP, USA) as a specific surface area tester. The sample was degassed at 250 °C to remove water and impurities, followed by analysis in the analytical chamber. The entire analysis was conducted in a low-temperature zone where liquid nitrogen existed, with high-purity nitrogen and helium as the carrier gases. Finally, the sample was placed in an N_2 atmosphere, followed by physical adsorption on the sample surface and calculation of the pore size distribution using the Barrett-Joyner-Halenda (BJH) method.

The fabrication of the working electrode involved several steps. First, a specific quantity of chitosan was weighed and dissolved in water to create a solution with a 2 mg mL^{-1} concentration. Subsequently, an equivalent amount of the catalyst was weighed and dissolved in the chitosan solution at a 3 mg mL^{-1} concentration. Thereafter, the mixture was ultrasonically treated for 1 h. Subsequently, 60 µL of the treated mixture was pipetted onto the conductive surface of FTO (fluorine-doped tin oxide) glass, ensuring an even distribution to form a thin film. Subsequently, the thin film was placed in a vacuum oven and dried overnight at 100 °C. All electrochemical tests were performed on a CHI660E instrument (Chenhua, Shanghai) utilizing a three-electrode system. A Na_2SO_4 solution (0.2 mol L^{-1}) was employed as the electrolyte, with a 0.01-10^5 Hz frequency range and a 5 mV amplitude.

Synthesis of the photocatalyst

Synthesis of TiO_2

The synthesis of TiO_2 has been documented in the literature.[30] First, 3 mL of TBOT was dispersed in 100 mL of deionized water, followed by stirring at room temperature for 30 min to obtain a white precipitate. Subsequently, the precipitate was washed with deionized water and collected, followed by overnight drying in a vacuum oven at 80 °C.

Synthesis of g-C_3N_4

The synthesis of g-C_3N_4 has been reported in the literature.[31] A precise quantity of urea was introduced into a porcelain boat and calcined at 550 °C within an N_2 atmosphere for 4 h, with a heating rate of 2.3 °C min^{-1}, to obtain a yellow powder, which was subsequently collected and reserved.

Synthesis of TCN

A specific quantity of TiO_2 was dispersed in 50 mL of deionized water and subjected to ultrasonic dispersion for 1 h. Subsequently, a designated amount of g-C_3N_4 was incorporated into the mixed solution and ultrasonically dispersed for 1 h. Subsequently, the mixture was transferred to ice water, followed by the dropwise addition of 30 mL of H_2O_2 solution (30%) within 1 h. Subsequently, this mixture was transferred to a Teflon-lined stainless-steel autoclave and kept at 130 °C for 24 h. Upon reaction completion, the resulting precipitate was meticulously washed with deionized water until no H_2O_2 was detectable. Finally, the precipitate was dried overnight at 80 °C in a vacuum oven. For 0.3, 0.6, 0.9, 1.2, and 1.5% of g-C_3N_4 added, the variations were denoted as 0.3TCN, 0.6TCN, 0.9TCN, 1.2TCN, and 1.5TCN, respectively.

RESULTS AND DISCUSSION

Fourier transform infrared spectroscopy (FTIR)

FTIR was employed to characterize the functional groups within molecular structure. For pure g-C_3N_4, the characteristic absorption

peak between 3000 and 3440 cm^{-1} was attributed to the N–H bond stretching vibration, and the peak at 1200-1640 cm^{-1} corresponded to the C_6N_7 unit stretching vibration.[32] The peak at 810 cm^{-1} was attributed to the triazine unit stretching vibration.[33] As far as the TiO_2 molecule is concerned, the distinct peak at 670 cm^{-1} signified the Ti–O stretching vibration. However, TiO_2 and g-C_3N_4 exhibited characteristic absorption peaks in the composite material, but the peak associated with g-C_3N_4 was less pronounced due to its low doping concentration.

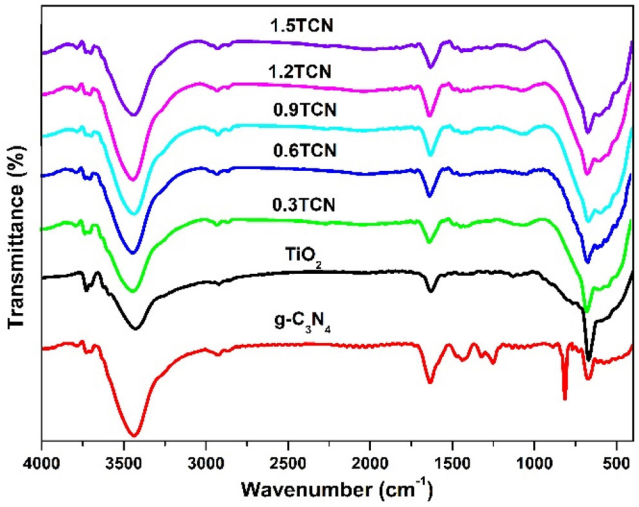

Figure 1. *FTIR spectra of xTCN*

X-ray powder diffraction (XRD)

The XRD patterns of xTCN are presented in Figure 2. Notably, g-C_3N_4 exhibited a distinct diffraction peak at 21.8° due to the interference of the instrument. The characteristic diffraction peaks of g-C_3N_4 were at 12.3° and 27.3° (Joint Committee on Powder Diffraction Standards (JCPDS) No. 87-1526). However, the characteristic peaks for g-C_3N_4 had diminished intensities due to the interference peak. The characteristic diffraction peaks of g-C_3N_4 were indicative of the in-plane stacking of the tri-triazine units and the interlayer conjugated aromatic ring.[34] The distinctive diffraction peaks of TiO_2 were identified at 25.3, 37.19, 48.04, 53.88, 55.06, and 62.68°, which corresponded to the (101), (004), (220), (105), (211), and (204) crystal planes, respectively. A comparison with the standard card (JCPDS No. 65-5714) confirmed the successful synthesis of TiO_2. In the composites, the crystal planes of TiO_2 were preserved, but the exposed crystal plane of g-C_3N_4 was not distinctly visible, primarily due to its low content.

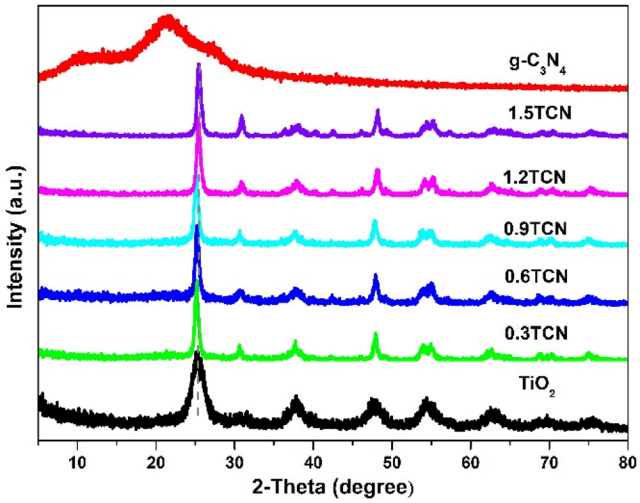

Figure 2. *XRD patterns of xTCN*

Scanning electron microscopy (SEM)

The macromorphology of the samples was illustrated using SEM. As shown in Figure 3a (32.00k× magnification), TiO_2 had a blocky structure with a relatively smooth surface. As shown in Figure 3b (52.00k× magnification), g-C_3N_4 appeared flaky when it was calcined in urea. The 0.9TCN (18.00k× magnification) surface was characterized by thin nanosheets, which essentially enveloped the bulk TiO_2 structure. The close contact between the two materials confirmed the successful synthesis of the photocatalyst composite.

Ultraviolet-visible diffuse reflectance spectroscopy (UV-Vis DRS)

The ultraviolet-visible (UV-Vis) absorption spectra of xTCN are presented in Figure 4. The g-C_3N_4 had a UV absorption edge at 459.3 nm, demonstrating strong visible light absorption. Conversely, TiO_2 and xTCN had absorption edges at 387.5 nm, aligning with the absorption edge of visible light and exhibiting robust UV light absorption. The bandgap determined using the Kubelka-Munke equation was 2.88, 3.22, and 3.29 eV for g-C_3N_4, TiO_2, and xTCN, respectively.

Photoluminescence (PL)

The transfer of photogenerated electrons between materials was investigated using the PL spectrum. Generally, a lower fluorescence intensity in a material indicates a reduced composite effect of energy loss and an increased photocatalytic activity. The PL spectra of

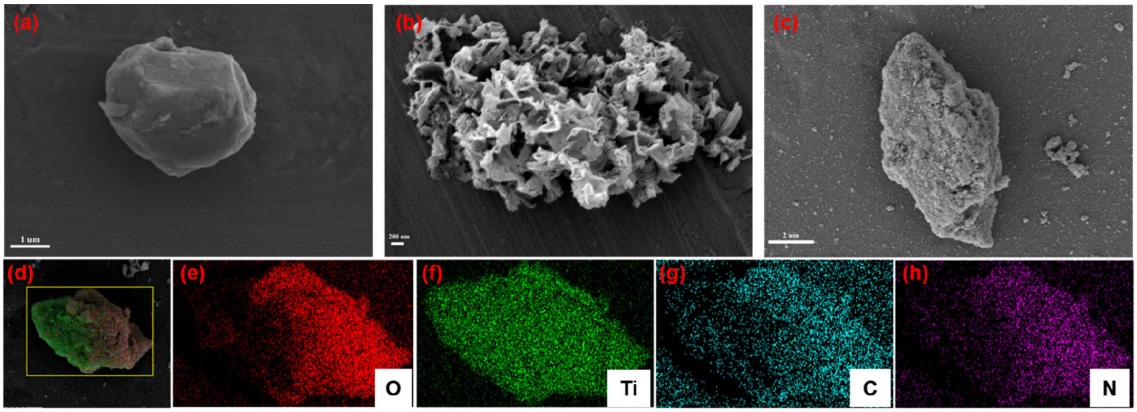

Figure 3. *SEM images of (a) TiO_2, (b) g-C_3N_4, and (c) 0.9TCN. (d-h) EDS mappings of 0.9TCN*

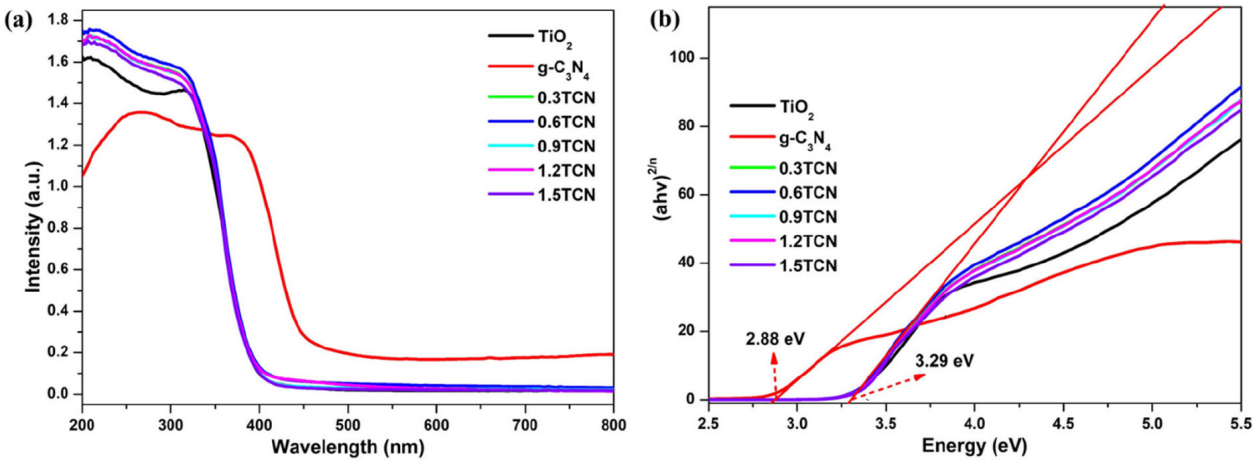

Figure 4. *(a) UV-Vis absorption spectra and (b) Tauc plots for xTCN*

xTCN and the composite materials are presented in Figures 5a and 5b, respectively. The excitation of g-C_3N_4 using UV light resulted in the rapid recombination of photogenerated carriers, exhibiting strong fluorescence intensity. Additionally, TiO_2, a typical semiconductor material, demonstrated strong fluorescence intensity when excited by UV light. However, the combination and oxidation of these two materials with H_2O_2 significantly reduced their fluorescence intensities. Consequently, this further confirmed the formation of a heterojunction between TiO_2 and g-C_3N_4, which enhanced the migration efficiency of the photogenerated carriers and improved the photocatalytic activity of the materials.

Electrochemical impedance spectroscopy (EIS)

The photoelectric performance of photocatalytic materials could be assessed using electrochemical methods, such as electrochemical AC (alternating current) impedance, which provided an accurate reflection of the photogenerated electron-hole separation efficiency. Generally, a smaller radius of curvature in the material corresponded to higher photogenerated electron-hole separation efficiency and enhanced photocatalytic activity. The radius of curvature of the materials followed the order: 0.9TCN < 1.5TCN < g-C_3N_4 < TiO_2 < 0.6TCN < 1.2TCN < 0.3TCN. Therefore, the material with the smallest radius of curvature exhibited the highest photogenerated electron-hole separation efficiency, leading to superior photocatalytic performance when 0.9% g-C_3N_4 was added (Figure 6).

X-ray photoelectron spectroscopy (XPS)

The elemental composition and chemical state of each element within a material is frequently determined using XPS. The composition of 0.9TCN was Ti, O, C, and N elements, with elemental proportions of 23.67, 54.55, 18.07, and 3.71%, respectively (Figure 7a). The high contents of O and C elements were attributed to the interference from O_2 and CO_2. The characteristic Ti $2p_{3/2}$ and Ti $2p_{1/2}$ peaks were at 458.67 and 464.47 eV, respectively, due to the spin-orbit splitting photoelectron energy level of the Ti element. The difference in energy levels, Δ = E $2p_{1/2}$ – E $2p_{3/2}$ = 5.8 eV, indicated the presence of Ti^{4+} in the compound (Figure 7b).[35] The peaks at 529.47 and 529.97 eV were attributed to the lattice O and the peroxide group, respectively (Figure 7c).[36] The peaks at 530.37 and 531.77 eV corresponded to surface hydroxyl and water molecules adsorbed on the TiO_2 surface.[37] Additionally, the peak at 530.07 eV was produced by H_2O_2. The peak at 284.79 eV corresponded to the carbon pollution from the unstable surface of the environment (Figure 7d). The peaks at 285.77 and 288.17 eV belonged to the C=N groups and sp^3 hybrid C with $(N)_2$–C=N in g-C_3N_4, indicating the successful synthesis of urea in a graphite-like form.[38] The peak at 285.17 eV binding energy was attributed to the Ti–O–C group. The characteristic peak at 398.07 eV binding energy originated from the N atom in the triazine ring (CN=C), and the characteristic peak at 399.87 eV corresponded to the tertiary nitrogen group (N-$(C)_3$). Therefore, the two forms of N constituted the main g-C_3N_4 structure, forming a large delocalized π bond. The characteristic peak at 400.47 eV was the amino group at the g-C_3N_4 layer edge.[39]

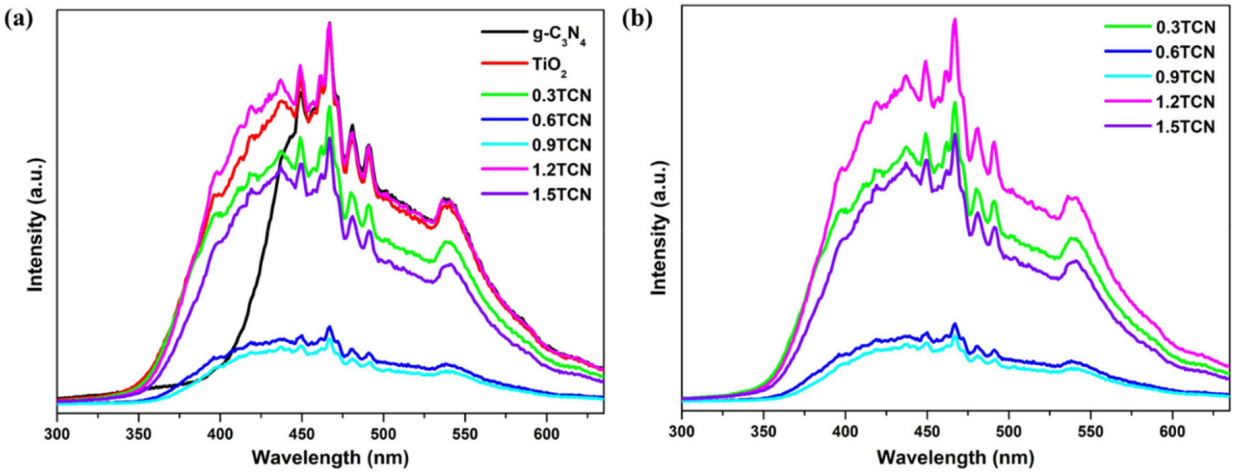

Figure 5. *PL spectra of xTCN*

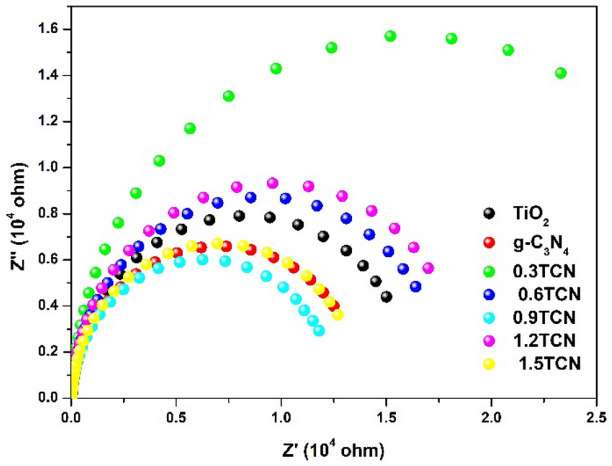

Figure 6. *EIS Nyquist plot of xTCN*

Brunauer-Emmett-Teller specific surface area (S_{BET})

The S_{BET} N_2 adsorption-desorption curve was utilized to measure the specific surface area and aperture of the material, and the corresponding specific surface area and other data were calculated using the BJH method. As shown in Figure 8a, TiO_2 exhibited a typical IV isotherm and an H2-type hysteresis loop. This phenomenon primarily arose from the strong interaction between the adsorbate molecules and the surface. The adsorption capacity rapidly increased, and the curve became convex under pressure. Multilayer adsorption gradually occurred as the relative pressure continued to increase, leading to infinite adsorption layers. Consequently, determining the precise limit of the equilibrium adsorption value under saturated vapour pressure in the experiment was challenging. However, the curve demonstrated a revival in its latter segment and introduced a hysteresis loop within the central section, which corresponded with the capillary condensation observed in porous adsorbents. When

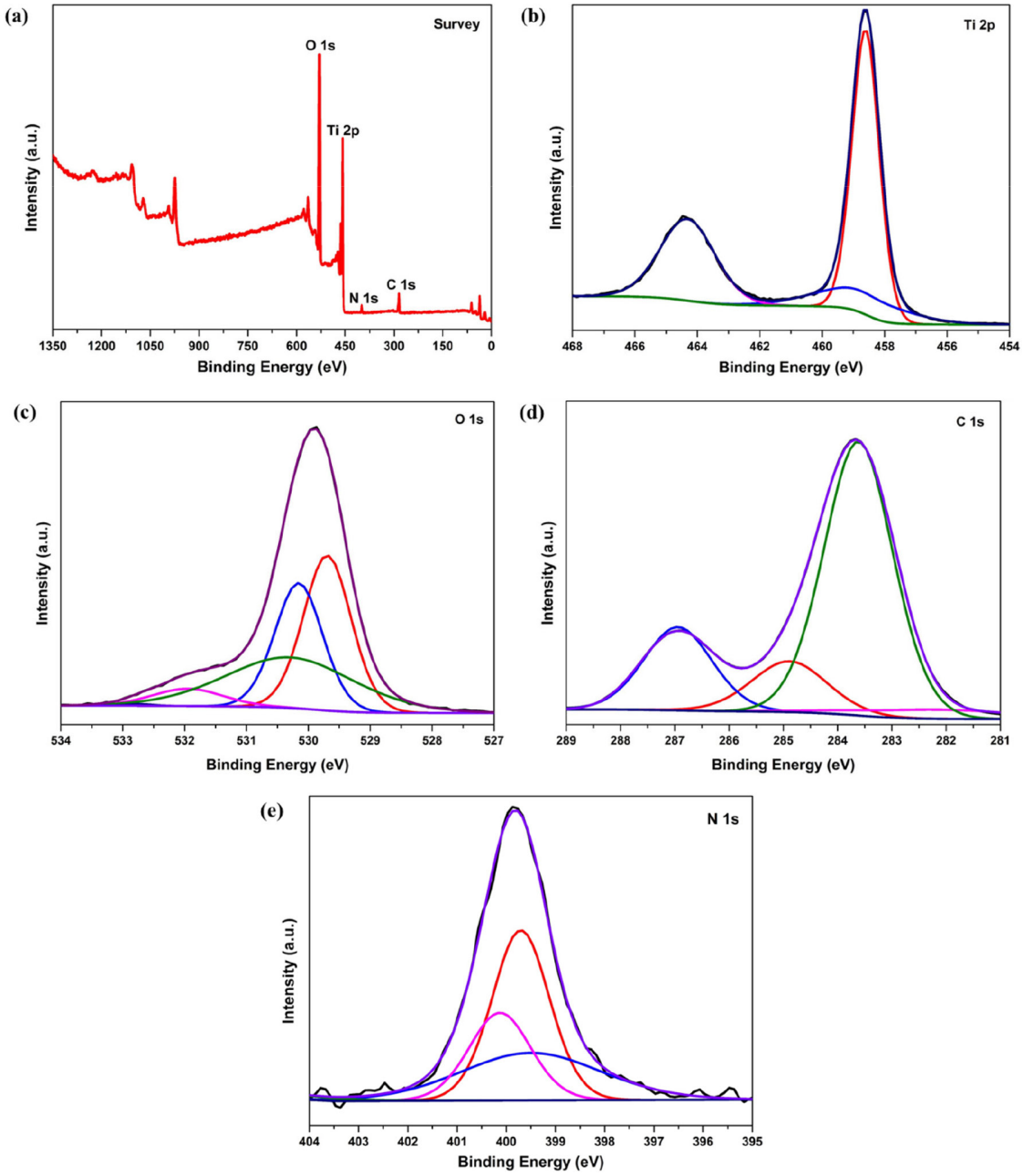

Figure 7. *XPS spectra of 0.9TCN (a). The survey at Ti 2p (b), O 1s (c), C 1s (d), and N 1s (e)*

the mesopores are saturated through capillary condensation, the adsorbent could continue to adsorb if it contained large diameter pores or the interaction forces among adsorbate molecules were strong, forming multi-molecular layers. Consequently, this led to the adsorption isotherm maintaining an upward trajectory. However, most instances would have an adsorption termination platform, and no further multilayer adsorption would occur after the capillary condensation. The BET analysis (Figure 8b) demonstrates a high linear correlation (R = 0.9999), exceeding the threshold for valid BET interpretation (R > 0.995). As shown in Figures 8c and 8e, g-C_3N_4 and 0.9TCN had type III isotherms with an H3-type hysteresis ring. The isotherm displayed an inflexion point, indicating that the quantity of the adsorbed gas increased proportionally with the partial pressure of the components. The curve was concave due to a strong interaction between the adsorbent molecules and the adsorbate, making it difficult for the adsorbent molecules to adsorb initially. However, it self-accelerated as adsorption progressed, and there was no limit to the number of adsorption layers. The H3 hysteresis rings suggested that the molecules had irregular pore structures, and the molecules did not reach adsorption saturation in the higher relative pressure areas. Figures 8d and 8f shows an excellent BET fitting correlation (R = 0.9999), satisfying the accuracy requirement (R > 0.995). The specific surface area, pore diameter, and total pore volume of the materials are summarized in Table 1. Compared to TiO_2, 0.9TCN had a reduced specific surface area but increased pore diameter and total pore volume. As seen in Table 1, the increased content of

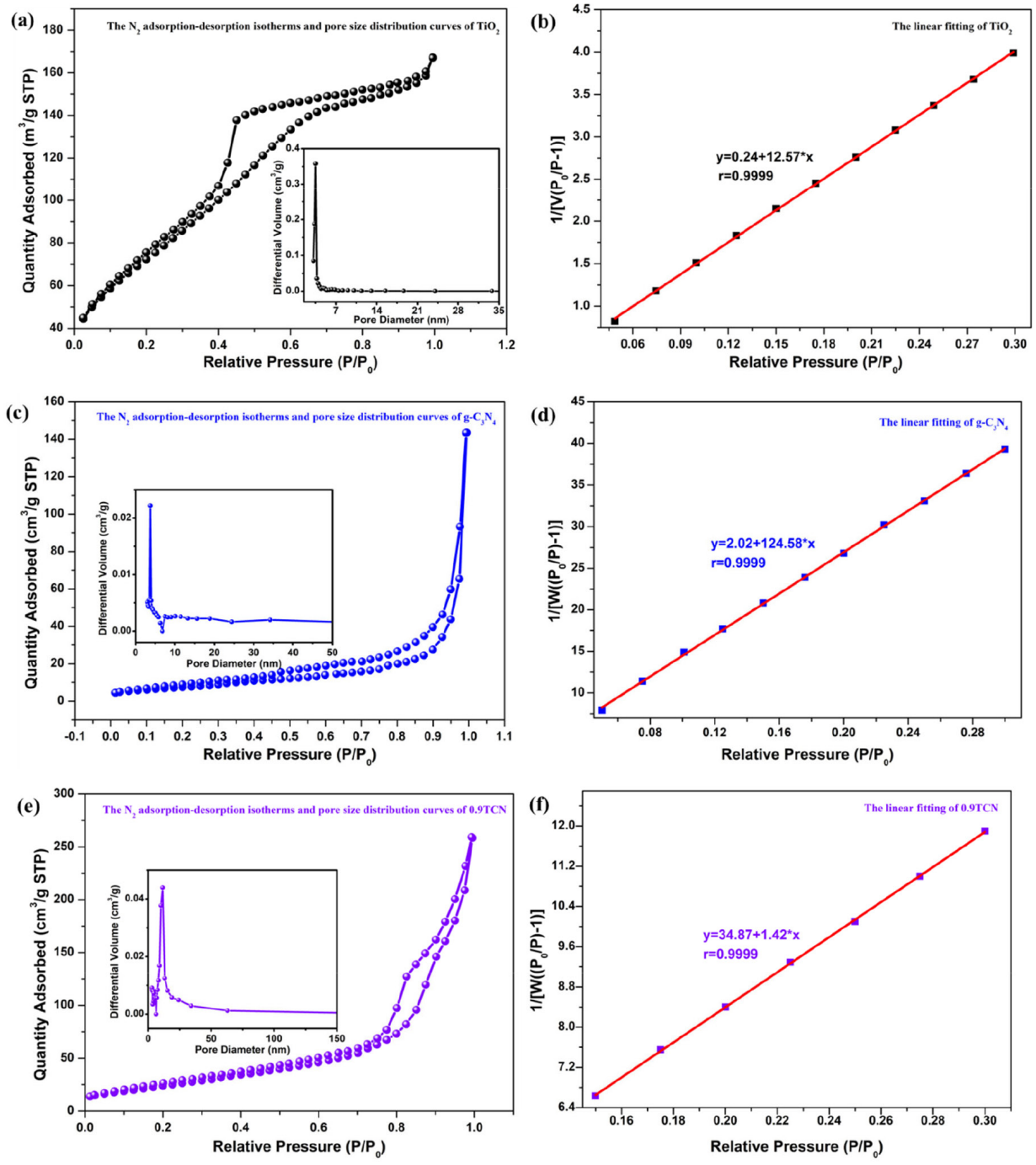

Figure 8. *(a) N_2 adsorption-desorption isotherms, pore size distribution curves, and (b) linear fitting of TiO_2; (c) N_2 adsorption-desorption isotherms, pore size distribution curves, and (d) linear fitting of g-C_3N_4; (e) N_2 adsorption-desorption isotherms, pore size distribution curves, and (f) linear fitting of 0.9TCN*

Table 1. Pore structure data for the samples from BET

Catalyst	Surface area / (m^2 g^{-1})	Average pore diameter / nm	Total pore volume / (cm^3 g^{-1})
TiO_2	272.16	3.8	0.259
g-C_3N_4	27.54	32.3	0.223
0.9TCN	108.9	16.7	0.401

g-C_3N_4 in TiO_2 correspondingly increased the ratio of macropores to macropores within the photocatalyst due to the inherent porosity of g-C_3N_4. Consequently, the TiO_2 nanoparticles were integrated into the layered structure of g-C_3N_4, which modified the atomic arrangement of the N–C bond and optimized the π-conjugate structure of g-C_3N_4.

Photocatalytic activity

The catalytic activity of the xTCN photocatalyst was examined by choosing the selective oxidation of benzalcohol as the model reaction. Compared to TiO_2 and g-C_3N_4, the composite materials significantly enhanced the conversion of benzalcohol, with the conversion varying significantly depending on the amount of g-C_3N_4 added. When 0.9% of g-C_3N_4 was added, the conversion of benzalcohol reached 77%, with the selectivity exceeding 99%. Concurrently, the conversion of benzalcohol was investigated in the absence of a catalyst, O, and under dark conditions. As shown in Table 2, benzalcohol essentially did not convert without a catalyst, O, or under dark conditions. However, the conversion of benzalcohol was low when only a catalyst was added in the absence of oxygen or when only O was added in the absence of a catalyst. Therefore, it could be concluded that a catalyst and O were essential for the selective catalytic oxidation of benzalcohol.

Table 2. Photocatalytic oxidation of benzalcohol with different catalysts

Catalyst[a]	Atmosphere condition	Light source	Conversion[b] / %	Selectivity[c] / %
TiO_2	O_2	yes	25	78
g-C_3N_4	O_2	yes	12	92
0.3TCN	O_2	yes	43	95
0.6TCN	O_2	yes	48	> 99
0.9TCN	O_2	yes	77	> 99
0.9TCN	/	yes	22	> 99
0.9TCN	O_2	/	5	/
/	O_2	yes	2	> 99
1.2TCN	O_2	yes	59	> 99
1.5TCN	O_2	yes	41	97

[a]Reaction conditions: benzalcohol (0.1 mmol), catalyst (5 mg), ethyl acetate (6 mL), 300 W metal halide lamp irradiation, light for 5 h, and room temperature; [b,c]calculated using GC analysis. /: absence of a reaction condition.

Furthermore, the impact of solvents on the photocatalytic reaction was surveyed by selecting various polar solvents to facilitate the selective oxidation of benzalcohol. As shown in Table 3, strong polar solvents, such as ethanol, were detrimental to the reaction and decreased the activity for the selective oxidation of benzalcohol. Conversely, moderate polar solvents, like ethyl acetate and acetonitrile, enhanced the reaction and led to increased activity. However, other moderate and weakly polar solvents and non-polar solvents, like 1,2-dichloroethane and CCl_4, adversely affected the reaction and reduced its activity. The reaction proceeded more smoothly in aprotic polar solvents, likely because they facilitated the transfer of photogenerated electrons and improved the separation efficiency of the photogenerated carriers. Consequently, these solvents exhibited pronounced solvating effects.

Table 3. Photocatalytic oxidation of benzalcohol in different solvents

Entry[a]	Solvent	Conversion[b] / %	Selectivity[c] / %
1	ethanol	5	25
2	acetonitrile	65	88
3	ethyl acetate	77	> 99
4	THF	15	40
5	toluene	11	4
6	hexane	32	48
7	1,2-dichloroethane	18	> 99
8	carbon tetrachloride	18	24

[a]Reaction conditions: benzalcohol (0.1 mmol), catalyst (5 mg), solvent (6 mL), 300 W metal halide lamp irradiation, light for 5 h, O_2 and room temperature; [b,c]calculated using GC analysis; THF: tetrahydrofuran.

Furthermore, this study selected benzalcohol derivatives as the subject matter since the versatility of a catalyst is crucial for broadening its range of applications. The conversion of the oxidation reaction was found to be higher when the benzalcohol substituents were linked to an electron-donating group. Conversely, the conversion of the substrate was lower when the substituents were connected to an electron-withdrawing group. Interestingly, the conversion of the benzohydrol derivatives was low regardless of whether the substituents were attached to an electron-donating or electron-withdrawing group. Consequently, this suggested that the electronic effect only influenced the benzalcohol derivatives and did not impact the benzohydrol derivatives.

Reusability

The study of the reusability of photocatalysts is crucial for heterogeneous and homogeneous catalysis. After five consecutive uses, the conversion of benzalcohol using xTCN decreased by 16%, while the selectivity for benzaldehyde only dropped by 9%. Consequently, this suggested that the photocatalyst exhibited superior photostability (Figure 9a). A comparison of the FTIR spectra and XRD patterns of the photocatalysts pre- and post-reaction showed no significant alterations in the molecular structure. Specifically, the characteristic absorption peak of 0.9TCN remained unchanged in the FTIR spectra, indicating that the light reaction did not compromise the molecular integrity of the photocatalyst. Similarly, the characteristic diffraction peak of the photocatalyst was unaltered in the XRD pattern. Therefore, these findings underscored the photostability and recyclability of the photocatalyst.

Reaction mechanism

The proposed reaction mechanism for the selective oxidation of benzalcohol was investigated using the Mott-Schottky curve (M-S curve) analysis and active-species trapping experiments. Various active species trapping agents were introduced to the reaction system in the experimental setup to identify the active species involved in the photocatalytic reaction. Specifically, Na_2SO_3, $AgNO_3$, IPA, BQ, TEMPO, and N_2 were employed to distinguish the roles of holes (h^+), electrons (e), OH radical, O_2^- radical, and O_2 in the reaction system, respectively. The conversion of benzalcohol and the selectivity towards benzaldehyde were unaltered when Na_2SO_3 and $AgNO_3$

Table 4. Photocatalytic oxidation of the benzalcohol derivatives using 0.9TCN under visible light

Entry[a]	Substrate	Product	Conversion[b] / %	Selectivity[c] / %
1	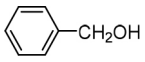	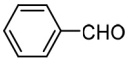	76	> 99
2	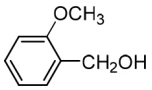	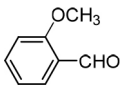	69	85
3	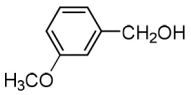	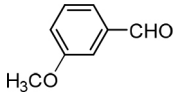	63	75
4	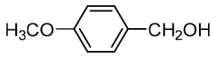	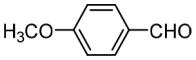	72	95
5	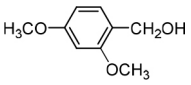	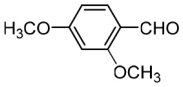	78	> 99
6	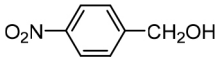	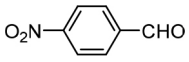	4	83
7	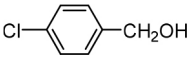	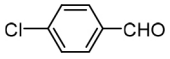	39	68
8	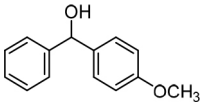	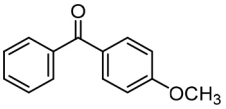	54	85
9	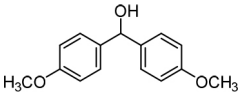	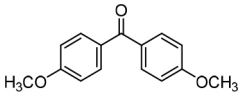	26	40
10	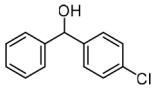	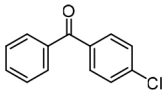	10	56
11	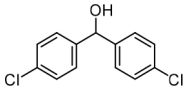	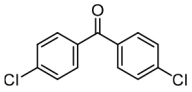	11	65

[a]Reaction conditions: benzalcohol derivatives (0.1 mmol), catalyst (5 mg), ethyl acetate (6 mL), 300 W metal halide lamp irradiation, light for 5 h, O_2, and room temperature; [b,c]calculated using GC analysis.

were introduced to neutralize h^+ and *e,* indicating that h^+ and *e* were not the primary active species. The conversion of benzalcohol and the selectivity of benzaldehyde were slightly reduced upon treatment with IPA, suggesting that the OH radical was involved in the photoreaction. The addition of TEMPO to the reaction system significantly decreased the conversion of benzalcohol, underscoring the crucial role of radicals in its oxidation. The photocatalyst exhibited a near-complete deactivation in the N_2 atmosphere, highlighting the necessity of O_2 for the photocatalytic oxidation of benzalcohol. In summary, the $\bullet O_2^-$ and •OH radicals were the predominant active species in the oxidation of benzalcohol.

As seen in Figure 10, the slope of the M-S curve for 0.9TCN was positive, indicating that TCN composites were n-type semiconductors.[40] This was consistent with previous reports[41] indicating that the conduction band potential was more negative than the flat band potential (0.1). As measured using the M-S curve with a 0.2 mol electrolyte and Ag/AgCl as the reference electrode, the flat band potential of 0.9TCN was –0.97 eV. Consequently, the conduction band potential of 0.9TCN was found to be –0.46 eV compared to the potential of $O_2/\bullet O_2^-$ (–0.33 eV), inferring that the composites could reduce O_2 to $\bullet O_2^-$ by photoinduction. As a result, this finding aligned with the results obtained from the active species-capture experiments. Based on UV-Vis absorption spectra, the bandgap determined was 3.2 eV. Additionally, using an experimental formula, the calculated valence band was 2.74 eV. This potential could generate OH radicals, a conclusion that was also supported by the results of the active species-capture experiments. Therefore, it could be concluded that the $\bullet O_2^-$ and •OH radicals were the primary active species.

CONCLUSIONS

The TCN composite photocatalysts were synthesized using a hydrothermal method with H_2O_2 as the oxidant. The photocatalysts exhibited optimal catalytic performance when 0.9% of g-C_3N_4 was added, resulting in a 77% conversion of benzalcohol and more than 99% selectivity for benzaldehyde. Ethyl acetate proved to be the most suitable solvent, and the photocatalyst demonstrated strong applicability (specifically for benzyl alcohol derivatives) within this photoreaction system. After five cycles of recycling, the conversion of benzalcohol and the selectivity for benzaldehyde dropped by only 16 and 9%, respectively, indicating that the photocatalyst had outstanding reusability. Furthermore, the photocatalyst had a largely unchanged molecular structure before and after illumination, confirming its excellent photostability. Mechanistic studies revealed that $\bullet O_2^-$ and

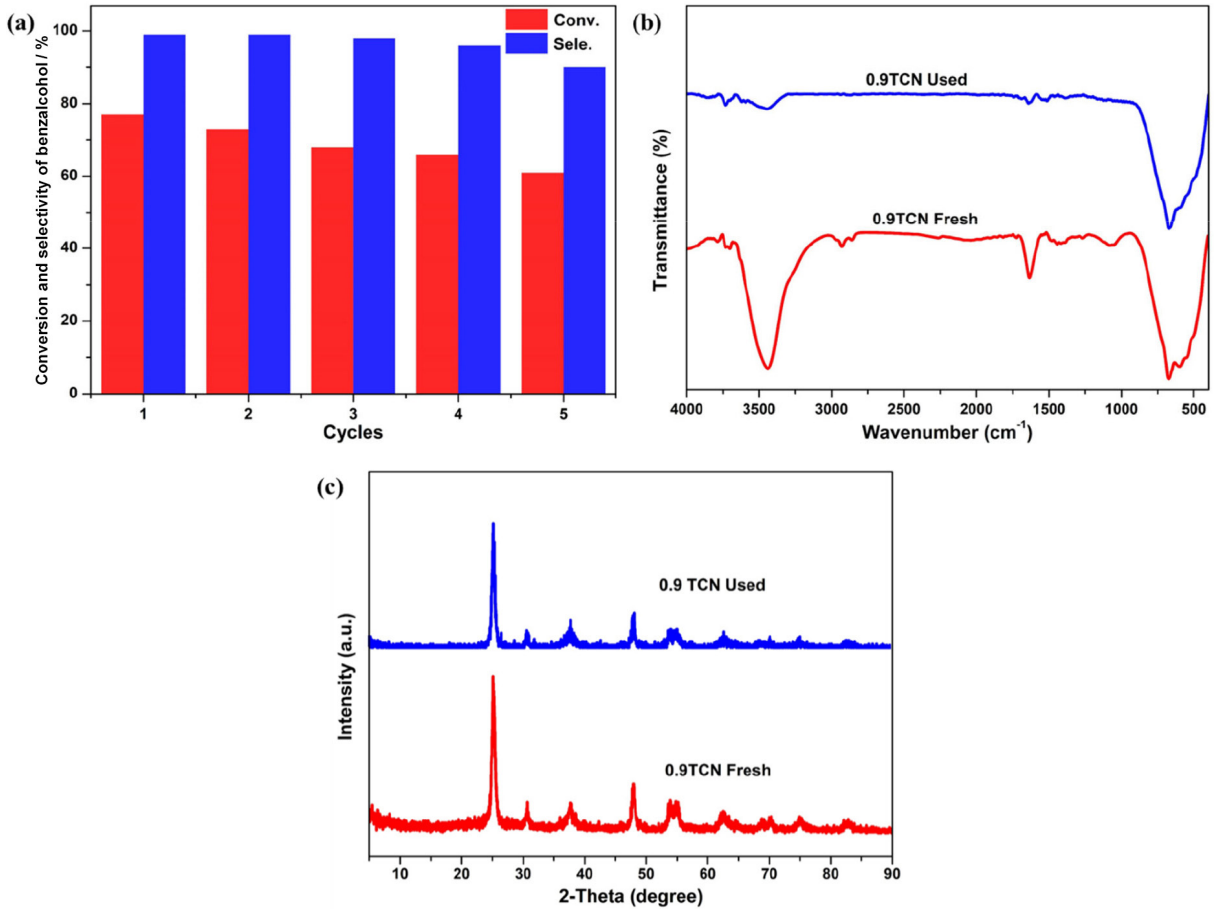

Figure 9. *(a) Reusability of 0.9TCN; (b) FTIR spectra; (c) XRD patterns of the fresh and used photocatalyst*

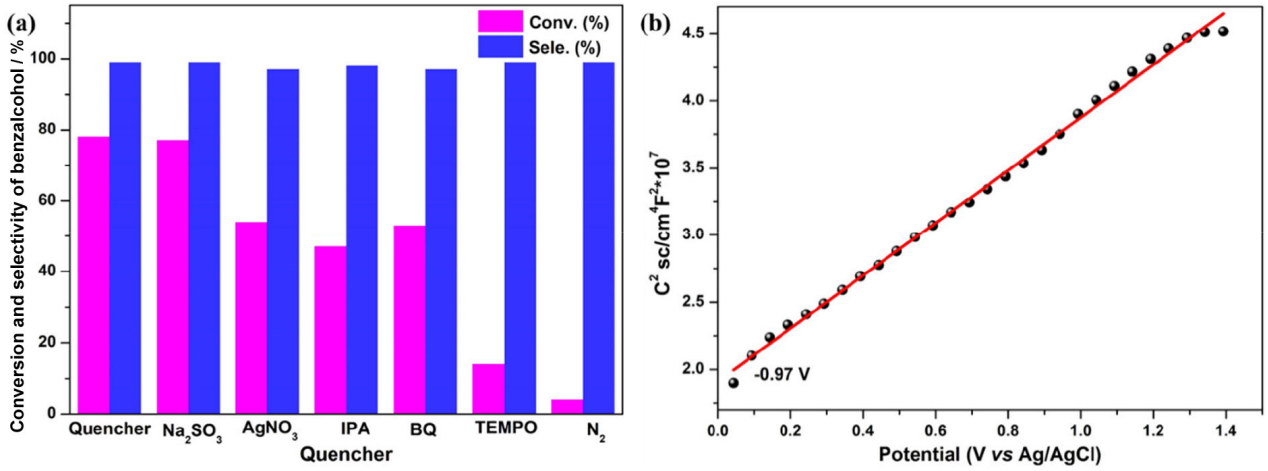

Figure 10. *(a) Effects of the scavengers of different reactive species on the photocatalytic oxidation of benzalcohol and (b) M-S curve of xTCN*

•OH were the primary active species responsible for the selective oxidation of benzalcohol.

DATA AVAILABILITY STATEMENT

All data are available within the text.

ACKNOWLEDGMENTS

The research was financially supported by the Science and Technology Program of Gansu Province, China (grant No. 23JRRA1666), the Special Fund for Talent Introduction and Scientific Research of Gansu Academy of Sciences, China (grant No. QD2023-05), the Youth Fund Program of Gansu Academy of Sciences (grant No. 2024QN-15), and the Longyuan Youth Innovation and Entrepreneurship Talent Program.

AUTHOR CONTRIBUTIONS

Shuangyan Meng was responsible for the data curation, validation, funding acquisition, writing - original draft, writing - review and editing; Bin Liu for the formal analysis; Minglin Xie for the investigation; Chaoxin Yun for the investigation; Jin Qiang for the resources; Kaizhou He for the project administration; Zhiwang Yang for the conceptualization, funding acquisition, writing - review and editing; Xiangqian Wang for the project administration.

REFERENCES

1. Pina, C. D.; Falletta, E.; Ross, M.; *J. Catal.* **2008**, *260*, 384. [Crossref]
2. Guo, Z.; Liu, B.; Zhang, Q. H.; Deng, W. Q.; Wang, Y.; Yang, Y. H.; *Chem. Soc. Rev.* **2014**, *43*, 3480. [Crossref]
3. Parmeggiani, C.; Matassini, C.; Cardona, F.; *Green Chem.* **2017**, *19*, 2030. [Crossref]
4. Bao, X. L.; Li, H. L.; Wang, Z. Y.; Tong, F. X.; Liu, M.; Zheng, Z. K.; Wang, P.; Cheng, H. F.; Liu, Y. Y.; Dai, Y.; Fan, Y. C.; Li, Z. Y.; Huang, B. B.; *Appl. Catal., B* **2021**, *286*, 119885. [Crossref]
5. Kim, H.; Jo, S.; Lee, T. S.; *Mater. Des.* **2021**, *3*, 109630. [Crossref]
6. Wu, J.; Qi, M. X.; Wang, G.; Yu, B.; Liu, C. D.; Hou, W.; Liu, W. S.; *ACS Sustainable Chem. Eng.* **2020**, *8*, 5200. [Crossref]
7. Bian, J. C.; Huang, C.; Wang, L. Y.; Hung, T. F.; Daoud, W. A.; Zhang, R. Q.; *ACS Appl. Mater. Interfaces* **2014**, *6*, 4883. [Crossref]
8. Wang, Z. M.; Huang, X. Q.; Jia, Y.; Guo, L. N.; Wang, H.; Dai, W. X.; *Chem. Eng. J.* **2024**, *482*, 148942. [Crossref]
9. Liu, S. C.; Zhou, Q. L.; Wen, D.; Wu, C. Y.; Pan, Y. Q.; Liu, X.; Huang, Z.; Li, N.; *ACS Catal.* **2024**, *14*, 8105. [Crossref]
10. Hu, Z. Z.; Wu, H. Z.; Li, S. S.; Zhang, C. H.; Liang, R. H.; Zhou, M. H.; *Chem. Eng. J*. **2024**, *498*, 155308. [Crossref]
11. Zou, X.; Yan, Z. R.; Tang, D. F.; Fan, S. C.; Peng, D. L.; Jiang, Y. L.; Wei, Q. L.; *J. Mater. Chem. A* **2024**, *12*, 13770. [Crossref]
12. Wang, X. G.; Liu, X. W.; Liu, L. H.; Hao, Y. F.; Zhou, Z. M.; Chen, F. J.; Pan, H. H.; Liu, Q. Y.; Liang, Y.; Zhang, Y. R.; Wang, P.; *Appl. Catal., B* **2024**, *358*, 124338. [Crossref]
13. Feng, G. H.; Mao, J. N.; Sun, T.; Li, G. H.; Li, S. J.; Dong, X.; Song, Y. F.; Wei, W.; Chen, W.; *ACS Appl. Mater. Interfaces* **2024**, *16*, 4600. [Crossref]
14. Impemba, S.; Provinciali, G.; Filippi, J.; Salvatici, C.; Berretti, E.; Caporali, S.; Banchelli, M.; Caporali, M.; *Int. J. Hydrogen Energy* **2024**, *63*, 896. [Crossref]
15. Padmanabhan, N. T.; Thomas, N.; Louis, J.; Mathew, D. T.; Ganguly, P.; John, H.; Pillai S. C.; *Chemosphere* **2021**, *271*, 129506. [Crossref]
16. Hidalgo, M. C.; Maicu, M.; Navío, J. A.; Colón, G.; *J. Phys. Chem. C* **2009**, *113*, 12840. [Crossref]
17. Choi, J.; Park, H.; Hoffmann, M. R.; *J. Phys. Chem. C* **2010**, *114*, 783. [Crossref]
18. Rao, Z. P.; Lu, G. H.; Mahmood, A.; Shi, G. S.; Xie, X. F.; Sun, J.; *Appl. Catal., B* **2021**, *284*, 119813. [Crossref]
19. Ding, S. J.; Yin, X.; Lü, X. J.; Wang, Y. M.; Huang, F. Q.; Wan, D. Y.; *ACS Appl. Mater. Interfaces* **2012**, *4*, 306. [Crossref]
20. Kong, W. Q.; Zhang, X. F.; Chang, B. B.; Zhou, Y. N.; Zhang, S. R.; He, G. L.; Yang, B. C.; Li, J. J.; *Electrochim. Acta* **2018**, *282*, 767. [Crossref]
21. Ong, W. J.; Tan, L. L.; Ng, Y. H.; Yong, S. T.; Chai, S. P.; *Chem. Rev.* **2016**, *116*, 7159. [Crossref]
22. Dong, J.; Shi, Y.; Huang, C. P.; Wu, Q.; Zeng, T.; Yao, W. F.; *Appl. Catal., B* **2019**, *243*, 27. [Crossref]
23. Zeng, G. H.; Wang, X. J.; Yu, X.; Guo, J.; Zhu, Y.; Zhang, Y. M.; *J. Power Sources* **2019**, *444*, 227300. [Crossref]
24. Zhao, N.; Kong, L.; Dong, Y.; Wang, G.; Wu, X.; Jiang, P.; *ACS Appl. Mater. Interface*s **2018**, *10*, 9522. [Crossref]
25. Zhang, W. J.; Xu, D. T.; Wang, F. J.; Chen, M.; *J. Alloys Compd.* **2021**, *868*, 159266. [Crossref]
26. Mao, Z. Y.; Chen, J. J.; Yang, Y. F.; Bie, L. J.; Fahlman, B. D.; Wang, D. J.; *Carbon* **2017**, *123*, 651. [Crossref]
27. Fu, J. W.; Xu, Q. L.; Low, J. X.; Jiang, C. J.; Yu, J. G.; *Appl. Catal., B* **2019**, *243*, 556. [Crossref]
28. Li, G. Y.; Nie, X.; Chen, J. Y.; Jiang, Q.; An, T. C.; Wong, P. K.; Zhang, H. M.; Zhao, H. J.; Yamashita, H.; *Water Res.* **2015**, *86*, 17. [Crossref]
29. Li, G. Y.; Nie, X.; Gao, Y. P.; An, T. C.; *Appl. Catal., B* **2016**, *180*, 726. [Crossref]
30. Wang, Y. P.; Liu, L.; Wu, D. J.; Guo, J.; Shi, J. Y.; Liu, J. M.; Su, C. Y.; *Chin. J. Catal.* **2019**, *40*, 1198. [Crossref]
31. Yu, W. L.; Chen, J. X.; Shang, T. T.; Chen, L. F.; Gu, L.; Peng, T. Y.; *Appl. Catal., B* **2017**, *219*, 693. [Crossref]
32. Xu, Q. L.; Zhu, B. C.; Jiang, C. J.; Cheng, B.; Yu, J. G.; *Sol. RRL* **2018**, *2*, 1800006. [Crossref]
33. Low, J. X.; Zhang, L. Y.; Tong, T.; Shen, B. J.; Yu, J. G.; *J. Catal.* **2018**, *361*, 255. [Crossref]
34. Pap, Z.; Danciu, V.; Cegled, Z.; Kukovecz, A.; Oszko, A.; Dombi, A.; Mogyorosi, K.; *Appl. Catal., B* **2011**, *101*, 461. [Crossref]
35. Gyulavari, T.; Pap, Z.; Kovacs, G.; Baia, L.; Todea, M.; Hernadi, K.; Vereb, G.; *Catal. Today* **2017**, *284*, 129. [Crossref]
36. Yuan, X.; Qu, S. L.; Huang, X. Y.; Xue, X. G.; Yuan, C. L.; Wang, S. W.; Wei, L.; Cai, P.; *Chem. Eng. J.* **2021**, *416*, 129148. [Crossref]
37. Wang, Y. C.; Zhou, J.; Hao, X. Q.; Wang, Y.; Zou, Z. G.; *Appl. Surf. Sci.* **2018**, *456*, 861. [Crossref]
38. Sun, L. P.; Niu, S. Y.; Jin, J.; Yang, G. D.; Ye, L.; *Eur. J. Inorg. Chem.* **2006**, *2006*, 5130. [Crossref]
39. Meng, S. Y.; Zeng, W.; Wang, M. M.; Niu, L. T.; Hu, S. P.; Su, B. T.; Yang, Y. X.; Yang, Z. W.; Xue, Q. J.; *New J. Chem.* **2020**, *44*, 2102. [Crossref]
40. Tan, L. L.; Ong, W. J.; Chai, S. P.; Mohamed, A. R.; *Chem. Eng. J.* **2016**, *283*, 1254. [Crossref]
41. Dong, F.; Wu, L. W.; Sun, Y. J.; Fu, M.; Wu, Z. B.; Lee, S. C.; *J. Mater. Chem.* **2011**, *21*, 15171. [Crossref]